Nanoscale

Nanoscale

www.rsc.org/nanoscale

ROYAL SOCIETY OF CHEMISTRY

www.rsc.org/nanoscale

Journal Name

ARTICLE

Superparamagnetic versus blocked states in aggregates of Fe$_{3-x}$O$_4$ nanoparticles studied by MFM

Carlos Moya,[*‡a] Óscar Iglesias-Freire,[‡b,c] Xavier Batlle,[a] Amilcar Labarta [a] and Agustina Asenjo [b]

Magnetic domain configurations in two samples containing small aggregates of Fe$_{3-x}$O$_4$ nanoparticles of about 11 and 49 nm in size, respectively, were characterized by magnetic force microscopy (MFM). Two distinct magnetic behavior were observed depending on particle size. Aggregates constituted of nanoparticles about 11 nm in size showed uniform dark contrast on MFM images, reflecting the predominant superparamagnetic character of those particles and arising from the coherent rotation of the spins within the aggregate as the latter align along the tip stray-field. Applying a variable in-plane field, it is possible to induce a magnetic polarization yielding an increasing dark/bright contrast as the strength of the applied field overcomes the stray-field of the tip, although this polarization completely disappears as the remanent state is back recovered when the magnetic field is switched off. On the contrary, for aggregates of NPs of about 49 nm in size, dark/bright contrast associated with the existence of magnetic domains and magnetic polarization prevails on MFM images all along of the magnetic cycle due to the blocking state of the magnetization of those larger particles, even in the absence of an applied field. All in all, we unambiguously demonstrate the capabilities of magnetic force microscopy to distinguish between blocked and superparamagnetic states in aggregates of magnetic nanoparticles. Micromagnetic simulations strongly support the conclusions stated from the MFM experiments.

Introduction

Magnetite nanoparticles (NPs) have been the focus of a lot of interest due to their easy production by chemical routes,[1] remarkable magnetic properties[2,3] and relative low toxicity;[4] all of them making these NPs suitable candidates for potential applications in biomedicine, such as contrast agents in magnetic resonance imaging (MRI),[5] drug delivery[6] and hyperthermia[7] among others,[8] and in technology, such as in magnetic recording.[9,10] In addition, they are ideal systems to study finite-size effects, yielding new phenomena and enhanced properties with respect to their bulk-counterparts.[11] One of the most common finite-size effects is superparamagnetism (SPM) which not only depends on the particle volume but it is also a time-dependent phenomenon due to the stochastic nature of the thermal activation energy.[11,12] Thus, for non-interacting particles, the observed magnetic behavior depends on the relative characteristic value of the acquisition time, τ_m, of the specific experimental technique with respect to the relaxation time, τ, associated with the probability of the spins to overcome the energy barriers for magnetic anisotropy.[11,12] In addition, SPM regime limits the use of NPs in several bioapplications and magnetic recording.[11] Consequently, special attention has

been paid to get an accurate dynamical magnetic characterization in order to distinguish between the SPM and blocked regimes of the net magnetization of NPs ensembles. The majority of those studies have been performed by measuring both DC (τ_m = 100s) and AC susceptibilities (τ_m = 10^{-1}-10^{-5}s for typical experiments), Mössbauer spectroscopy (τ_m = 10^{-7}-10^{-9}s) and neutron scattering (τ_m = 10^{-8}-10^{-12}s).[13,14]

A common downside of all these standard characterization techniques lies on the fact that they only provide average information over a very large number of NPs. On the contrary, the direct observation of either a single particle or small clusters of NPs is available by magnetic force microscopy (MFM).[15-19] MFM has proved to be a versatile technique, by means of which it is possible to study the real time evolution of the magnetic domains by variable-field MFM (VF-MFM)[20] or to characterize the evolution of MFM contrast versus tip-sample distance by 3D mode, allowing a complete characterization of small structures.[21,22] In addition, micromagnetic simulations performed with the Object Oriented Micromagnetic Framework (OOMF) code constitutes an ideal tool to interpret the experimental MFM images.[23]

Within this framework, we have addressed the study of SPM and blocked regimes of aggregates by MFM experiments in two samples of $Fe_{3-x}O_4$ NPs with mean diameters of 11 nm (R11) and 49 nm (R49), respectively, that were synthesized by thermal decomposition of organic precursors.[24,25] SPM and ferrimagnetic blocked NPs were independently observed and were fully differentiated for samples R11 and R49, respectively. Interestingly enough, 3D mode and VF-MFM experiments were carried out, aiming at studying the influence that the stray field emerging from the MFM tip has on the magnetic state of the sample, so as to avoid artifacts and misinterpretation of data when images corresponding to the SPM and blocked regimes were compared. Finally, micromagnetic simulations were used to gain some insight into the different mechanisms taking place during magnetization reversal.

Sample preparation

$Fe_{3-x}O_4$ NPs were prepared by high-temperature decomposition of Fe(III)-acetylacetonate with decanoic acid as capping ligand in an organic solvent, as reported elsewhere.[25,26] It has been shown that a wide range of monodisperse particle sizes can be obtained depending on the relative concentration of the reactants and temperature profile of the reaction.[25,26]

Sample R11. For 11 nm NPs, 5 mmol of decanoic acid were mixed with 1 mmol of Fe(III)-acetylacetonate in 25 mL of dibenzyl-ether. First of all, the solution was heated up to 200 ºC at a constant rate of 6.5 ºC/min under nitrogen atmosphere and vigorous stirring. After 2 h at 200 ºC, the reaction mixture was heated up to 270 ºC and kept at this temperature for 1 h. Finally, the solution was cooled down to room temperature, washed three times with ethanol and NPs were collected by centrifugation at 9000 rpm.

Sample R49. NPs 49 nm in size were obtained following the same method explained before but with a larger molar ratio of decanoic acid to Fe(III)-acetylacetonate (1:4) and setting the temperature profile to 3.5 ºC/min for the last reaction stage. Samples were stored in ethanol until final use.

Structural and magnetic characterization

The samples were prepared for transmission electron microscopy (TEM) (MT80-Hitachi microscope) by placing one drop of a dilute NPs suspension onto a carbon-coated copper grid and drying at room temperature. The size distribution was analyzed by measuring at least 2000 particles and the resulting histograms were fitted to log-normal functions (see Fig. 1d-e and S1a-b, Supporting information). The particles in both samples were found to be faceted (see Fig. 1a-b) and single-crystal domains of 11 and 49 nm in mean size, respectively. The standard deviation of the size distribution were 6 nm for R11 and 30 nm for R49.

The crystalline phase of the iron oxide particles was identified by powder X-ray diffraction. The patterns were collected between 5º to 120º in 2θ in a PANalytical X'Pert PRO MPD diffractometer by using Cu Kα radiation, and they were indexed

to an inverse spinel structure (Fig. 1f). The mean particle diameters obtained from XRD data (D_{XRD}) were 11 ± 0.5 nm for R11 and 45 ± 2 nm for R49, in good agreement with estimations from TEM. This also confirms the high crystalline quality of the samples and their single-crystal domain features. The organic fraction of the samples was evaluated by thermogravimetric analysis (TGA). Measurements were effected in a TGA-SDTA 851e/SF/1100 (Mettler Toledo) at a heating rate of 10 ºC/min from room temperature up to 800 ºC in nitrogen atmosphere (see Fig. S2, Supporting information). Hysteresis loops $M(H)$ were measured with a Quantum Design SQUID magnetometer at 300 K (see Fig. 1c) to study the coercive field (H_c) and saturation magnetization (M_s) under a maximum magnetic field of $\pm$ 50 kOe. M_s was obtained by extrapolation of the high-field region of $M(H)$ curves to zero magnetic field, assuming the high-field behavior,
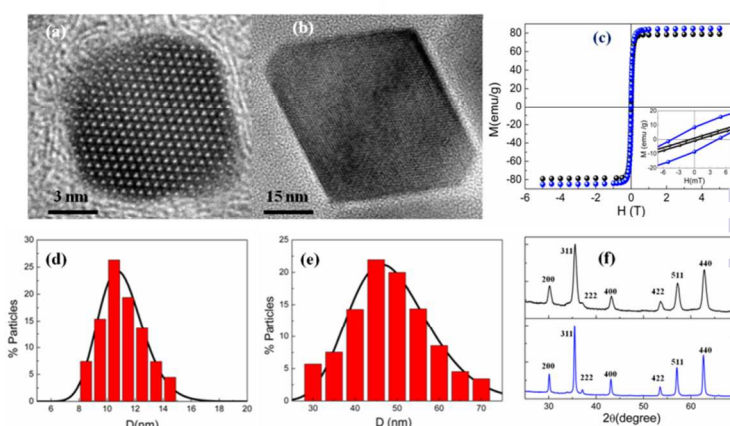

Figure 1. (a) and (b) HRTEM images of sample R11 and R49, respectively. (c) Hysteresis loops of $Fe_{3-x}O_4$ NPs at 300 K . Blue circles: sample R49, black circles: sample R11. Inset: detail of the low field region. (d) and (e) show the particle size distribution for R11 and for R49, respectively. (f) X-ray diffraction pattern with the indexation of the Bragg peaks to an inverse structure for R11 (black line) and for R49 (blue line).

$M(H) = M_s + \chi H$, where χ is a residual susceptibility.[3] M_s values were normalized to the magnetic content by subtracting the organic fraction evaluated by TGA analyses from the sample mass. The values obtained at RT were $M_s = 78.0 \pm 0.7$ emu/g for R11 and $M_s = 84.3 \pm 0.1$ emu/g for R49. Those values are just slightly smaller than the bulk one, indicating an almost perfect ferrimagnetic order throughout the whole NPs, as previously observed in samples with very high crystal quality synthesized by the thermal decomposition method.[2],[3],[13],[26] Besides, H_c was defined as $H_c = (|H_c^+| + |H_c^-|)/2$, where H_c^+ and H_c^- are the interceptions of the hysteresis loop with the positive and negative sides of the H-axis, respectively. A magnification of the field range where those interceptions take place is shown in the inset to Fig. 1c. The obtained values of the coercive field are 0.8 ± 0.3 mT for R11 and 4.3 ± 0.5 mT for R49. This very small value of H_c for R11 suggests that the majority of the particles in this sample are SPM at RT, in contrast with the case for R49 where the magnetization of most of the particles remains blocked.

Magnetic force microscopy

Characterization of the aggregates by MFM

Figure 2 shows the topography and MFM images at remanence (zero field) of several aggregates containing a few particles of samples R11 (Fig. 2a-d) and R49 (Fig. 2e-f) and the corresponding topographic and frequency shift profiles. The aggregates of the smaller R11 NPs give rise to a homogeneous attractive interaction between the tip and the sample, displayed as a uniform dark contrast in Fig. 2a-d, which is consistent with a coherent rotation of the spins within the NPs induced by the tip stray-field. This reflects the relatively low value of the net anisotropy energy arising from the small size of the R11 NPs and, consequently, their predominant SPM character.
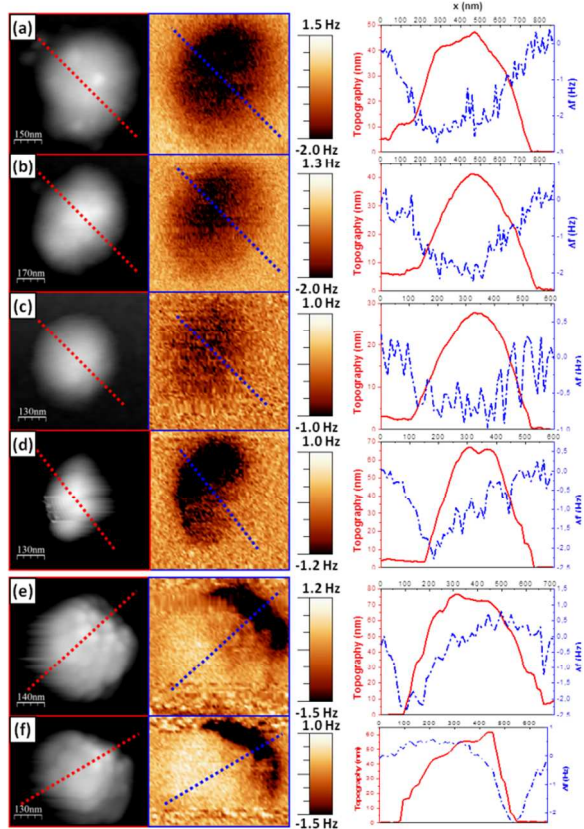

Figure 2. The remanent state. (a)–(f) Topographic *AFM* (left row) and *MFM* images (center row) of six different clusters of $Fe_{3-x}O_4$ NPs (R11: (a)-(d), R49: (e)-(f)), measured at remanence after in-plane magnetic saturation along the horizontal axis of the images. Right-most column: Heights (red solid line) and frequency shifts (blue solid line) profiles of the studied clusters (R11 and R49, respectively).

This kind of attractive tip-induced interactions is expected to occur in either SPM NPs or very soft magnetic nanostructures, the two cases not being unambiguously distinguishable by recording solely conventional MFM images. Therefore, care must be taken to avoid misinterpretation of the MFM data, as has been previously reported. [15,16,27,28] In order to confirm the SPM character of the aggregates of R11 NPs, a study of the dependence of the frequency shift on the tip-sample distance was carried out and the results are shown in Fig. 3.[21,22] To

perform this sort of experiments, the same profile across the aggregate is repeatedly scanned while the lift height is varied from 30 to 180 nm. As shown in Fig. 3d, the frequency shift decreases with the distance from (-1.23 ± 0.6) Hz at 30 nm to (-0.06 ± 0.42) Hz at 180 nm, accordingly to a monotonous reduction of the attractive interaction until the signal becomes comparable to the experimental noise. The latter reveals that the net magnetization of the R11 aggregates orients along the vertical direction even for very small values of the stray field emerging from the tip,[15] which in turn confirms the SPM character of these aggregates. However, aggregates of R49 NPs yield MFM images with well-defined magnetic polarity because of the blocked state of their net magnetization at RT (see Fig. 2e-f).

The characterization by MFM imaging of those aggregates has revealed two situations as regards to the interaction between the stray-fields of the tip (B_{tip}) and that generated by the sample (B_{sample}). For sample R11, $B_{tip} > B_{sample}$ and aggregates are observed to be in a SPM regime, while for sample R49, $B_{tip} < B_{sample}$ and a blocked state of the sample magnetization with well-defined magnetic polarity is clearly displayed on the MFM images.
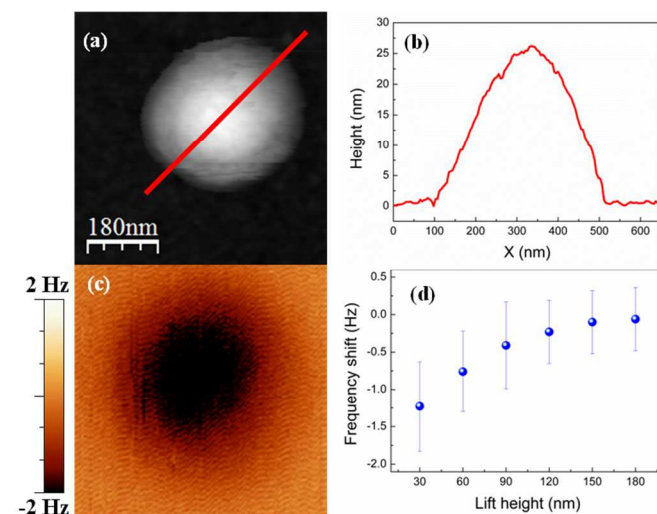

Figure 3. (a) Topography of a cluster of NPs for R11. (b) Height profile of the studied cluster. (c) MFM image of the cluster in (a). (d) Variation of the frequency shift from 30 to 180 nm lift height in a 3D experiment.

Variable field MFM study

A deeper insight into the magnetic nature of those particle aggregates can be gained by recording VF-MFM images as a function of an in-plane applied magnetic field. Results are shown in Fig. 4 for three cases recorded, respectively, at zero field and with a field of 82 mT applied in opposite in-plane directions. Similar magnetic domain structures with opposite polarities can be observed when comparing images at opposite values of the applied field for R11 aggregates (see Fig. 4a-d). Considering that these aggregates are SPM at zero field, the observed magnetic polarization can be understood as just

induced by the action of the external magnetic field, since the associated dark/bright contrast progressively disappears becoming only dark contrast as the magnitude of the field is decreased to zero (see central panels in Fig. 4a-d). So the in-plane polarization is imprinted in the aggregates when the strength of the applied field is large enough to overcome the attractive interaction between the sample and the stray-field of the tip. On the contrary, magnetic domains within the R49 aggregates are not totally saturated at 82 mT and non-symmetric states of the magnetization polarization are observed at both sides of the magnetic cycle (see Fig. 4e-f). At the same time, the dark/bright contrast prevails along the whole magnetic cycle since the net magnetization of these large particles remains blocked during the acquisition time of the MFM images.
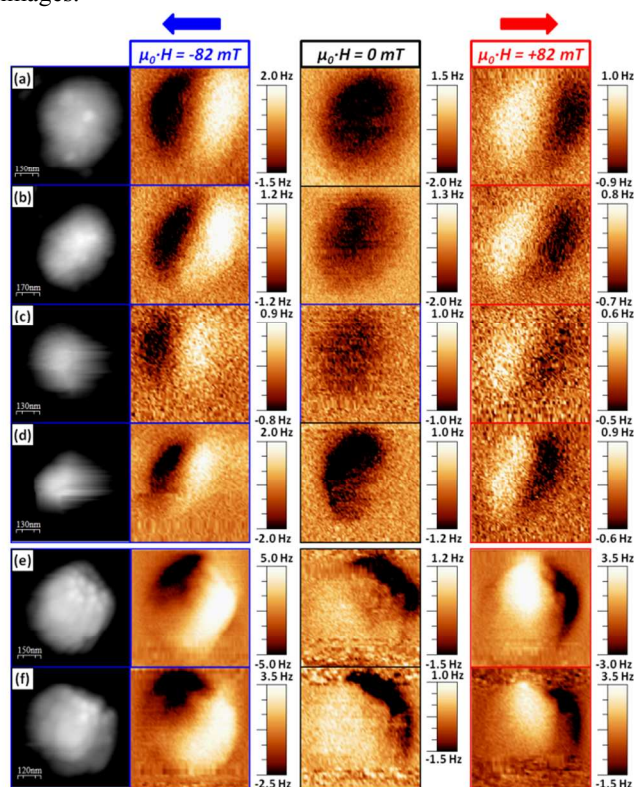

Figure 4. The domain polarity. Topographic (left) and MFM images (right) of the same NPs in Figure 2 (a)-(f) [(a)-(d) for R11 and (e)-(f) for R49], in the presence of in-plane horizontal magnetic fields with opposite direction (+/- 82 mT) and at zero magnetic field.

A detailed sequence depicting the reversal processes of the magnetic domains for the R49 aggregate shown in Fig. 4e is presented in Fig. 5a. A single domain configuration is observed at both sides of the magnetic cycle and along much of the way down to remanence, indicating that the aggregate behaves predominantly as a macro-spin. Interestingly, as the field direction is reversed from negative values a multi-domain structure is observed, where a domain wall seems to be present. That multi-domain structure defines the reversal process until a single domain configuration is reached again, with an uncompleted reversal of the magnetization polarity because the

magnitude of the maximum applied field is not enough to achieve complete saturation. Therefore, the larger volume of these aggregates and their multi-particle nature result in a domain wall-mediated reversal of the magnetization, as compared to the coherent rotation of spins taking place in isolated NPs, as reported elsewhere.[18]

Micromagnetic simulations

In order to gain further knowledge on the processes involved in magnetization reversal, micromagnetic simulations were carried out using the OOMMF free source software.[23] The 3D Oxsii mode was used with the following parameters: saturation magnetization, $MS = 4.66$ kA/m (obtained from the hysteresis loop shown in Fig. 1b); exchange stiffness constant for magnetite,[29] $A = 13.2 \cdot 10^{-12}$ J/m; magneto-crystalline anisotropy constant for bulk magnetite,[13] $k1 = 12$ kJ/m^3 and a cubic cell size of $(2x2x2)$ nm^3. One should recall here that micromagnetic simulations are known to reproduce with high reliability experimental results in a qualitative manner, lacking in general quantitative reproducibility of experiments. Reasons for this can be attributed to thermally activated processes, the influence of structural and/or surface effects.

Figure 5b presents a simulated distribution of the magnetization during the reversal process in a cluster of $(3x3)$ 50 nm-NPs with an additional one on the top of the middle of the square cluster. The external field was applied in-plane along the horizontal axis of the images. The apparent broadening of lateral dimensions intrinsic to AFM experiments mentioned above might cause such a cluster to appear with similar dimensions to the ones displayed in Fig. 4. The direction of the local magnetization is represented by arrows in a blue-red scale which indicates an outbound-inbound component (with respect to the image plane); the simulated MFM image is shown in a black-white scale which stands for a negative-positive divergence of the magnetization (thus, causing the appearance of the magnetic charges to which MFM is sensitive). The sample was initially saturated along the direction of negative polarity and magnetization reversal was studied.

Snapshots of the most relevant steps within the reversal process are shown in Fig. 5b. A single-domain phase is again first observed all the way from saturation to remanence (left image in Fig. 5b) and even for low fields applied upon reversal of the field direction. However, the relatively large lateral dimensions of this cluster of NPs allow for the magnetization to adopt a configuration with increasing in-plane curling. At a certain field value, a magnetic vortex is formed and magnetization reversal takes then place as the vortex moves across the cluster. The simulated MFM contrast emerging from this configuration reproduces up to a good extent the experimental results highlighted in Fig. 5a by green/yellow frames. Note that the exact orientation and shape of the experimental cluster may differ from those of the simulated one. Finally, a single (but reversed) domain is again obtained.

Therefore, our simulations suggest magnetization reversal to be mediated by nucleation and propagation of a vortex domain wall. Additional simulations were performed in

larger clusters of (4x4) NPs with another one on the top and the same mechanism was observed.
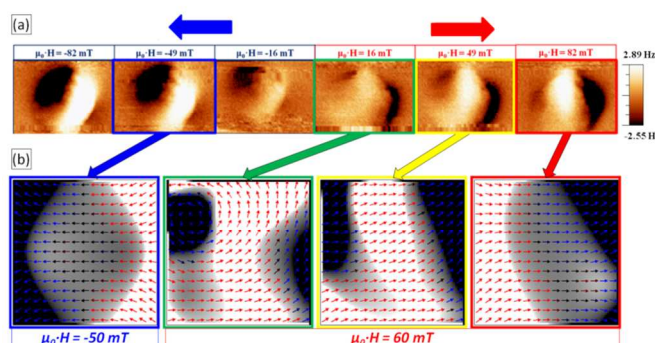

Figure 5. (a) MFM images of the aggregate shown in Fig. 4e in the presence of horizontal in-plane magnetic fields with variable magnitude and direction. (b) Results of the micromagnetic simulations, for a cluster of (3x3) 50 nm-NPs with an additional one on the top of the middle, showing various stages of the magnetization reversal, compared to the MFM images squared in (a) by color frames. The arrows and color code indicate the correspondence between the MFM images and the snapshots of the micromagnetic simulations.

Conclusions

MFM characterization of small aggregates of $Fe_{3-x}O_4$ NPs at RT reveals two distinct magnetic behavior depending on the particle size. Aggregates constituted of NPs about 11 nm in size show homogeneous attractive tip-sample interaction, displayed as a uniform dark contrast on the MFM images, and arising from the coherent rotation of the spins within the aggregate as they align along the tip stray-field. This reflects the predominant SPM character of those small particles observed within the characteristic acquisition time of the MFM technique and at zero applied field. Interestingly enough, applying a variable in-plane field, it is possible to induce a magnetic polarization yielding an increasing dark/bright contrast as the strength of the applied field increases and overcomes the stray-field of the tip. However, this induced polarization completely disappears as the remanent state is back recovered when the applied field is switched off. On the contrary, for aggregates of NPs of about 49 nm in size, dark/bright contrast associated with the existence of magnetic domains and magnetization polarization prevails on MFM images all along of the magnetic cycle, since the net magnetization of these large particles remains blocked during the acquisition time of the MFM images even at zero applied field. Therefore, the larger volume of these aggregates and their multi-particle nature yield a domain-wall mediated reversal of the magnetization, as compared to the coherent rotation of spins taking place in either aggregates of SPM NPs or even isolated particles with blocked magnetization. Micromagnetic simulations suggest such walls to be formed by an in-plane magnetic vortex moving across the cluster.

Experimental Section

MFM measurements were carried out at RT using a VF-MFM set-up from Nanotec Electrónica.[30] All experiments were performed using the lift mode (lift height: 40 nm), in which the topographic profile is retraced at a tip-sample distance for which magnetostatic interactions become dominant. MFM data arise from the change in the resonance frequency of the oscillating cantilever induced by such magnetostatic coupling between the tip and sample. In all the experiments performed, a phase-locked loop (PLL) was used to keep a constant phase lag between the driving signal and the cantilever oscillation, so that MFM data have units of Hz. BudgetSensors Multi75-G tips were used, with nominal values of the spring constant k≈3N/m and resonance frequency f_0≈75 kHz.

Samples for MFM observations were prepared by placing one drop of a dilute suspension of NPs onto a carbon-silicon wafer and letting it dry in an oven at 348 K for 1 h in order to remove all the remaining solvent. All images were collected at 0.5 lines/s and with a resolution of 256x256 pixels, so that the acquisition time was 7.8 ms/pixel. Taking this into account, an estimation of the maximum size for an isolated particle showing SPM behavior can be calculated by assuming a typical Néel relaxation of the magnetization with an relaxation time of about τ_0 = 10^{-9}-10^{-11}s and an anisotropy constant of K_v = 2-$4 \cdot 10^5$ erg·cm^{-3}, within the typical values found in magnetite NPs.[31,32] As result, a critical particle size of 11-16 nm is estimated for the observation of the SPM regime in our MFM data (see S3, Supporting information). Thus, NPs with smaller dimensions will exhibit SPM behavior and, consequently, internal magnetic domain configurations will not be observable by MFM.

It is worth noting that AFM techniques are very accurate in measuring vertical distances, whereas lateral dimensions of protruding nanostructures are unavoidably overestimated due to the convolution of tip-sample interactions over the tip apex volume.[18]As a consequence, NPs appear wider than their real size, whereas this convolution effect is not present in vertical displacements of the tip, which yields particle heights (see Fig. 2e-h) in outstanding agreement with the TEM size histogram shown in Fig. 1d-e. Corresponding topographic and MFM images display the exact same location; however, magnetic features may appear offset from the topographic ones, as different regions of the tip are sensitive to interactions with the sample during either AFM or MFM imaging (see Figure S4, Supporting information).

Notes and references

[a] Departament de Física Fonamental, Institut de Nanociència i Nanotecnologia, Universitat de Barcelona, Barcelona, 08028, Spain

[b] Instituto de Ciencia de Materiales de Madrid (ICMM-CSIC), Cantoblanco, Madrid, 28049 Spain

[c] Department of Physics, McGill University, Montreal, H3A 2T8, Canada

*Corresponding author E-mail: cmoya@ffn.ub.es

‡ These two authors contributed equally.

† Electronic Supplementary Information (ESI) available: PDF material contains TEM images for samples R11 and R49 (Figure S1), Thermogravimetric curves for samples R11 and R49 (Figure S2) and Calculated relaxation time from Arrhenius law for a single $Fe_{3-X}O_4$ NP following Néel relaxation (Figure S3).

1 A. G. Roca, R. Costo, A. F. Rebolledo, S. Veintemillas-Verdaguer, P. Tartaj, T. González-Carreño, M. P. Morales, C. J. Serna, *J. Phys. D. Appl. Phys.* 2009, **42**, 224002.

2 P. Guardia, B. Batlle-Brugal, a. G. Roca, O. Iglesias, M. P. Morales, C. J. Serna, a. Labarta, X. Batlle, *J. Magn. Magn. Mater.* 2007, **316**, e756.

3 P. Guardia, A. Labarta, X. Batlle, *J. Phys. Chem. C* 2011, **115**, 390.

4 Y. Zhang, N. Kohler, M. Zhang, *Biomaterials* 2002, **23**, 1553.

5 H. Bin Na, I. C. Song, T. Hyeon, *Adv. Mater.* 2009, **21**, 2133.

6 M. Arruebo, R. Fernández-Pacheco, M. R. Ibarra, J. Santamaría, *Nano Today* 2007, **2**, 22.

7 R. Mejías, S. Pérez-Yagüe, A. G. Roca, N. Pérez, A. Villanueva, M. Cañete, S. Mañes, J. Ruiz-Cabello, M. Benito, A. Labarta, X. Batlle, S. Veintemillas-Verdaguer, M.P. Morales, D.F. Barber, C. J. Serna, *Nanomedicine*. 2010, **5**, 397.

8 Q. A. Pankhurst, J. Connolly, S. K. Jones, J. Dobson, *J. Phys. D. Appl. Phys.* 2003, **36**, R167.

9 S. Wang, F. J. Yue, D. Wu, F. M. Zhang, W. Zhong, Y. W. Du, *Appl. Phys. Lett.* 2009, **94**, 012507.

10 S. Yun, B. Sohn, J. C. Jung, W. Zin, *Langmuir* 2005, **14**, 6548.

11 X. Batlle, A. Labarta. Journal of Physics D: Applied Physics. 2002, **35**, R15.

12 C. P. Bean, J. D. Livingston, *J. Appl. Phys.* 1959, **30**, S120.

13 B. D. Cullity, C. D. Graham, *Introduction to Magnetic Materials*, **2011**.

14 I. Prigogine, S. A. Rice, Eds. , *Advances in Chemical Physics*, John Wiley & Sons, Inc., Hoboken, NJ, USA, **1997**.

15 C. S. Neves, P. Quaresma, P. V Baptista, P. a Carvalho, J. P. Araújo, E. Pereira, P. Eaton, *Nanotechnology* 2010, **21**, 305706.

16 S. Schreiber, M. Savla, D. V Pelekhov, D. F. Iscru, C. Selcu, P. C. Hammel, G. Agarwal, *Small* 2008, **4**, 270.

17 S. Sievers, K.-F. Braun, D. Eberbeck, S. Gustafsson, E. Olsson, H. W. Schumacher, U. Siegner, *Small* 2012, **8**, 2675.

18 C. Moya, Ó. Iglesias-Freire, N. Pérez, X. Batlle, A. Labarta, A. Asenjo, *Nanoscale* 2015, **7**, 8110.

19 P.Ares, M.Jaafar,A. Gil, J. Gómez-Herrero,A. Asenjo, *Small* **2015**. (DOI: 10.1002).

20 M. Jaafar, J. Gómez-Herrero, A. Gil, P. Ares, M. Vázquez, A. Asenjo, *Ultramicroscopy* 2009, **109**, 693.

21 C. Gómez-Navarro, F. Moreno-Herrero, P. J. de Pablo, J. Colchero, J. Gómez-Herrero, A. M. Baró, *Proc. Natl. Acad. Sci. U. S. A.* 2002, **99**, 8484.

22 M. Jaafar, L. Serrano-Ramón, O. Iglesias-Freire, A. Fernández-Pacheco, M. R. Ibarra, J. M. De Teresa, A. Asenjo, *Nanoscale Res. Lett.* 2011, **6**, 407.

23 Donahue MJ, Porter DG, National Technitian Information Service Document No. PB99 163214, National Institute of Standars and Technology (NIST), 1999 http://www.ntis.gov/Index.aspx.

24 P. Guardia, J. Pérez-Juste, A. Labarta, X. Batlle, L. M. Liz-Marzán, *Chem. Commun. (Camb).* 2010, **46**, 6108.

25 P. Guardia, N. Pérez, A. Labarta, X. Batlle, *Langmuir* 2010, **26**, 5843.

26 X. Batlle, N. Pérez, P. Guardia, O. Iglesias, A. Labarta, F. Bartolomé, L. M. García, J. Bartolomé, A. G. Roca, M. P. Morales, C. J. Serna, *J. Appl. Phys.* 2011, **109**, 07B524.

27 O. Iglesias-Freire, J. R. Bates, Y. Miyahara, A. Asenjo, P. H. Grütter, *Appl. Phys. Lett.* 2013, **102**, 022417.

28 M. Jaafar, O. Iglesias-Freire, L. Serrano-Ramón, M. R. Ibarra, J. M. de Teresa, A. Asenjo. *Beilstein Journal of Nanotechnology*. 2011, **2**, 552.

29 Wu, H.-C.; Arora, S. K.;Mryasov, O. N.; Shvets, I. V. *Appl. Phys. Lett.* 2008, **92**, 182502.

30 http://www.nanotec.es

31 N. Pérez, P. Guardia, a G. Roca, M. P. Morales, C. J. Serna, O. Iglesias, F. Bartolomé, L. M. García, X. Batlle, a Labarta, *Nanotechnology* 2008, **19**, 475704.

32 A. G. Roca, M. P. Morales, K. O'Grady, C. J. Serna, *Nanotechnology* 2006, **17**, 2783.